

21 **Abstract:** We develop a model for sheared gouge layers that accounts for the local increase in
22 temperature at the grain contacts during sliding. We use the shear transformation zone (STZ)
23 theory, a statistical thermodynamic theory, to describe irreversible macroscopic plastic
24 deformations due to local rearrangements of the gouge particles. We track the temperature
25 evolution at the grain contacts using a one dimensional heat diffusion equation. At low
26 temperatures, the strength of the asperities is limited by the flow strength, as predicted by
27 dislocation creep models. At high temperatures, some of the constituents of the grains may melt
28 leading to the degradation of the asperity strength. Our model predicts a logarithmic rate
29 dependence of the steady state shear stress in the quasi-static regime. In the dense flow regime
30 the frictional strength decreases rapidly with increasing slip rate due to the effect of thermal
31 softening at the granular interfaces. The transient response following a step in strain rate includes
32 a direct effect and a following evolution effect, both of which depend on the magnitude and
33 direction of the velocity step. In addition to frictional heat, the energy budget includes an
34 additional energy sink representing the fraction of external work consumed in increasing local
35 disorder. The model links low-speed and high-speed frictional response of gouge layers, and
36 provides an essential ingredient for multiscale modeling of earthquake ruptures with enhanced
37 coseismic weakening.

38

39

40

41

42

43 **I. Introduction**

44 Understanding the dynamics of shear weakening in gouge layers, under a wide range of slip rates
45 and confining normal stresses, is a fundamental and long-standing challenge in earthquake
46 source physics. In the case of mature faults, that have accumulated hundreds of meters of slip
47 throughout their active history, there is little doubt that shear deformation localizes to very thin
48 zones typically less than 1mm wide [Chester, 1993; Chester and Chester, 1998; Chester et al.,
49 2004; Noda and Shimamoto, 2005; Lockner et al., 2000; Ben-Zion and Sammis, 2003]. The zone
50 which accommodates most of the slip within this layer can be even smaller. The absence of
51 significant evidence of melting [Sibson, 1973; Lachenbruch, 1980], despite the extreme
52 localization of strain, suggests that fault friction must be low during dynamic sliding [Kanamori
53 and Heaton, 2000]. The fact that the static strength of fault gouge satisfies Byerlee's law (static
54 friction coefficient 0.6-0.9), however, indicates that faults are statically strong. Understanding
55 the mechanisms of dynamic weakening, from high static friction to low sliding friction, is
56 essential for developing more accurate models of earthquake ruptures and scenarios for ground
57 motion prediction [Rice, 1980, 2006; Heaton, 1990; Lapusta, 2000; Aagaard and Heaton, 2008;
58 Ampuero and Ben-Zion, 2008; Noda et al., 2009, 2010].

59

60 In this paper, we present a two-scale model for dynamic weakening in gouge layers.
61 Macroscopically, plastic strain results from the accumulation of local granular rearrangements.
62 Microscopically, thermally activated viscoplastic processes at the grain contacts control sliding
63 and force chain instabilities. The interplay between the two processes lead to non-monotonic
64 strain rate dependence for the shear strength.

65

66 Irreversible local rearrangements of gouge particles is modeled using the shear transformation
67 zone (STZ) theory, a continuum model of plastic deformation in amorphous solids that
68 quantifies local configurational disorder [Falk and Langer, 1998]. The basic assumption in the
69 theory is that plastic deformation occurs at rare non-interacting localized spots known as shear
70 transformation zones (STZs). An internal state variable, the effective temperature, describes
71 fluctuations in the configurational states of the granular material (i.e. a measure of local entropy),
72 and controls the density of STZs [Langer, 2004; Haxton and Liu, 2007; Langer and Manning,
73 2008; Bouchbinder and Langer, 2009]. Effective temperature can be related to the system
74 porosity [Lieou and Langer, 2012]. This approach coarse-grains granular simulations while
75 retaining important physical concepts.

76

77 Gouge particles with dimensions of a micrometer and above are too big for thermal fluctuations
78 to initiate transitions. Nonetheless, slip processes at the grain interfaces, such as dislocation glide
79 and stable crack growth, are thermally activated [Chester, 1994, Rice et al., 2001; Noda, 2008].
80 In particular, the high confining pressure at depths relevant to earthquake nucleation and
81 propagation lead to the prevalence of plastic conditions in the contact region. The local plastic
82 rheology depends strongly on the local temperature. Moreover, at high slip rates, flash heating
83 may occur leading to a significant degradation in the contact strength. Flash heating is the rapid
84 increase in local temperature at the contact asperity due to heat generation due to frictional
85 sliding at a rate higher than the heat diffusion rate [Rice, 2006]. By including the effect of local
86 temperature changes on the evolution of the flow strength at the particle interfaces, it is possible
87 to interpret the non-monotonic rate-dependent response of gouge layers observed experimentally

88 at different slip rates and normal stresses [Chester, 1994; Blanbied et al., 1995; Sone and
89 Shimamoto, 2009].

90

91 The primary result of this paper is the inclusion of a modified theory of flash heating within the
92 framework of the STZ theory, providing a mechanism for (i) rate strengthening in the quasistatic
93 regime of granular flow, and (ii) rate weakening in the dense regime of granular flow. This has
94 important geophysical implications for nucleation, dynamic rupture, and energy partitioning
95 during slip. The proposed theory is primarily relevant for small and moderate slips. For larger
96 slips the rise in macroscopic temperature, under seismological conditions, will be large enough
97 to cause macroscopic melting unless other weakening mechanisms such as pore fluid
98 pressurization operate.

99

100 The remainder of the paper is organized as follows. In Section II we review the basic elements of
101 the STZ theory. In Section III we discuss the model for local viscoplasticity at the grain contacts.
102 In Sections IV and V we describe the procedure for calculating the contact temperature for both
103 single and multiple contacts cases. In Section VI we discuss the parameter selection. In Section
104 VII we investigate the predictions of the STZ theory for the steady state sliding shear stress as
105 well as the transient behavior. We consider a wide range of strain rates. We also quantify the
106 partition of dissipated energy between configurational and thermal components. We conclude in
107 Section VIII by discussing implications of this model for dynamic rupture and gouge friction
108 modeling.

109

110 **II. A review of the STZ theory**

111

112 STZ theory is a non-equilibrium statistical thermodynamic framework for describing plastic
113 deformations in amorphous materials by quantifying local disorder. It has been successfully
114 applied to a variety of systems including granular fault gouge [Daub and Carlson, 2008; Daub et
115 al., 2008, Daub and Carlson, 2010, Hermundstad et al., 2010], glassy materials [Falk and Langer,
116 1998, 2000; Manning et al., 2007, 2009], thin film lubricants [Lemaitre and Carlson, 2004], and
117 hard spheres [Lieou and Langer, 2012]. In this section we review the basic assumptions and
118 equations of this theory.

119

120 Particles in amorphous materials can move and rearrange in response to applied stress. The total
121 shear deformation in any region can be approximated by two independent components; affine
122 motion, in which particle displacements are homogeneous, and non-affine motion, in which
123 particle displacements are inhomogeneous. Molecular dynamics simulations reveal that
124 nonaffine motion is concentrated in localized regions, called shear transformation zones (STZs).
125 These regions undergo configurational rearrangement by flipping between two bistable
126 orientations, anti-aligned and aligned, under applied shear stress [Falk and Langer, 1998].

127

128 A single STZ event generates, on average, a fixed amount of local plastic strain (ε) within the
129 material. The macroscopic plastic strain is the cumulative result of many local events. Once
130 flipped, STZs cannot further deform in the same direction. Instead, they are continuously created
131 and destroyed in order to further accommodate plastic strain within the material.

132

133 The amount of configurational disorder in the system is characterized by a single state variable:
 134 the effective temperature χ . The effective temperature is formally defined as the change in the
 135 system potential energy (or volume) per unit change in the system entropy [Bouchbinder and
 136 Langer, 2009; Lieou and Langer, 2012]. A fundamental result in the STZ theory is that the
 137 continuous creation and annihilation of the STZs drive their density Λ toward a Boltzmann
 138 distribution $\exp(-1/\chi)$ [Langer, 2008; Langer and Manning, 2008; Bouchbinder and Langer,
 139 2009].

140

141 The plastic strain rate $\dot{\gamma}$ is then given by:

$$142 \quad \dot{\gamma} = (\varepsilon_o/\tau_o) R(s, \chi) \exp(-1/\chi), \quad (1)$$

143 where ε_o is the average plastic strain increment per STZ, τ_o is a characteristic time scale and s is
 144 the shear stress. The rate at which STZs induce an infinitesimal plastic slip is given by the rate-
 145 switching function $R(s, \chi)$. The form of $R(s, \chi)$ is constrained by the second law of
 146 thermodynamics [Bouchbinder and Langer, 2009] and is given by:

147

$$148 \quad R(s, \chi) = \begin{cases} (1 - s_o/s) \exp(s/s_c \chi), & \text{if } s > s_o; \\ 0, & \text{if } s \leq s_o. \end{cases} \quad (2)$$

149 The parameters s_o and s_c are two stress scales for the STZ system. The stress parameter s_o is the
 150 minimum flow stress of the granular system. Thermal fluctuations are not sufficient to drive STZ
 151 reversal at the granular scale. Hence, $R(s, \chi)$ is nonzero only if $s > s_o$. Previously, it was shown
 152 that $s_c = p$ where p is the pressure [Lieou and Langer, 2012].

153 The effective temperature evolves according to the following equation:

$$\dot{\chi} = \frac{s\dot{\gamma}}{s_o c_o} \left(1 - \frac{\chi}{\hat{\chi}(\dot{\gamma})} \right) + \frac{\partial}{\partial z} D \dot{\gamma} \frac{\partial \chi}{\partial z}. \quad (3)$$

155

156 Equation (3) states that only a fraction of the externally applied work rate $s\dot{\gamma}$ is dissipated to
 157 increasing χ as it is driven toward its steady-state value $\hat{\chi}(\dot{\gamma})$ [Langer and Manning, 2008].

158 This fraction is given by $1 - \chi/\hat{\chi}$. The effective specific heat c_o determines the amount of
 159 energy required to increase the effective temperature. The second term on the RHS of Eqn. (3) is
 160 effective only if χ is spatially heterogeneous. There, D is the effective temperature diffusion
 161 coefficient and it scales with the square of particle size. Stability analysis [Manning et al., 2007]
 162 shows that the feedback between the strain rate and effective temperature may amplify spatial
 163 heterogeneities in the effective temperature and ultimately lead to shear banding. Homogeneous
 164 deformation corresponds to $\chi(z) = \text{constant}$, where z is the spatial coordinate across the gouge
 165 layer thickness.

166

167 The steady state effective temperature $\hat{\chi}(\dot{\gamma})$ satisfies the following condition: $d\hat{\chi}/dq \geq 0$ where
 168 $q = \dot{\gamma}\tau_o$ is the inertia number. Steady state simulations of glassy materials [Haxton et al., 2007;
 169 Langer and Manning, 2008] suggest that at high strain rates $\chi(\dot{\gamma})$ is given by:

$$\hat{\chi}(\dot{\gamma}) = \frac{A}{\ln(q_o/q)}, \quad (4)$$

171 where q_o is the inertia number at which the effective temperature diverges. In this limit the
 172 system fluidizes and a solid-like description like the STZ theory is no longer applicable. The
 173 value of q_o is estimated to be of the order 0.1-1 [Roux J.-N. and Chevoir F, 2005]. At low strain

174 rates, the steady state effective temperature can be approximated by a constant value χ_o that is
175 independent of strain rate. The rate parameter A determines whether the granular system is rate
176 strengthening or rate weakening. Numerous experimental and numerical models for systems of
177 hard and soft spheres under isothermal conditions predicts rate strengthening response [da Cruz
178 et al., 2005 and references therein]. We choose a value of A consistent with these observations.

179
180 A typical strain rate dependence for the steady state shear stress of a system of hard spheres is
181 shown in Fig. 1. No local plasticity at the grain level is considered and the system is assumed to
182 deform under isothermal conditions. Three major flow regimes are identified in this case. In the
183 quasi-static regime, prevailing at very low strain rates, the shear stress is almost independent of
184 the strain rate. In the dense regime the shear stress increases with increasing strain rate. In the
185 collisional flow regime, prevailing at high strain rates, kinetic energy due to collisional
186 interaction between the particles becomes no longer negligible and STZ theory breaks down. In
187 this limit, a hydrodynamic description is more relevant [Campbell, 1990].

188
189 The transition from quasistatic to dense flow depends on the properties of the granular system.
190 This is shown in Fig. 2 where the value of the parameter s_o is varied. The transition to dense
191 flow occurs at a higher inertia number for systems with higher s_o . Figure 2 suggests that varying
192 s_o alone not only alters the strength at low strain rates but it also leads to different strengthening
193 rates at intermediate and high strain rates.

194
195 The parameter s_o plays a central role in STZ theory. If a stress lower than s_o is applied to the
196 system, the system undergoes a transient deformation but it eventually stops. In this limit, the

197 force chains rearrange themselves and always find a stable configuration to resist the applied
198 stress. For stresses higher than s_o , the force chains continuously collapse and reform but no stable
199 configuration is achieved. Accordingly, a non-vanishing plastic strain rate is generated
200 [Bouchbinder and Langer, 2009; Lieou and Langer, 2012]. The value of s_o is a function of many
201 system variables such as grain shape and surface roughness, physical chemistry of the particles,
202 temperature and existence of fluids.

203

204 Different mechanisms contribute to flow resistance in granular systems. These include frictional
205 sliding, particle interlocking, and rolling friction. If the grains are not perfectly spherical, as it is
206 the case with most natural gouge particles, frictional sliding between particles dominate. In that
207 limit it is possible to relate the value of s_o to the local frictional strength, and hence viscoplastic
208 processes, at the grain contacts. To induce local plastic slip and rearrangements, a force chain
209 must buckle. This is possible if two particles in the chain slide relative to one another. This in
210 turn requires that the local stress at the particle interfaces exceeds the frictional strength. The
211 local stress and the macroscopic stress are related by:

212

$$213 \quad sA = s_l A_r, \quad (5)$$

214 where A is the apparent contact area (of order the particle cross sectional area), A_r is the real
215 contact area and s_l is the local stress at the contact level. Similarly, one may assume that the
216 parameter s_o is related to the flow strength at the contact level by an analogous relation:

$$217 \quad s_o A = s_{th} A_r, \quad (6)$$

218 where s_{th} is the flow strength at the contact level. Equation (6) establishes a correspondence
219 between the macroscopic yield stress s_o and the local flow strength:

$$220 \quad s_o = s_{th} \frac{A_r}{A}. \quad (7)$$

221 This is an important constraint for grains with viscoplastic contacts. Combining Eqns. (5) and (6)
222 we conclude that $s/s_o = s_l/s_{th}$. Accordingly, no persistent plastic deformation ($s > s_o$) is possible
223 unless the local frictional strength is exceeded. We discuss this further, in the context of other
224 contact models, in Sec V.

225
226 The ratio A_r/A depends on pressure s_c and the compressive strength of the grains. At the scale
227 of microcontacts, the compressive strength is of the order of the indentation hardness H of the
228 grains [Rice, 2006; Noda, 2008]. It then follows from equilibrium of normal stresses that
229 $A_r/A = s_c/H$. The indentation hardness depends on temperature; it decreases as the temperature
230 increases. We ignore the modest evolution of hardness as a function of temperature in this study.

231

232 **III. Viscoplasticity at the grain contacts**

233

234 To complete the temperature-dependent STZ model, we need to define an evolution law for the
235 local flow strength at the grain contacts. Different possible mechanisms for plastic deformation
236 at that scale exist. The dominant mechanism depends on many parameters such as temperature,
237 pressure and grain size. On the macroscopic scale, the granular system is amorphous with no
238 long range order associated with grain positions. Locally, however, the grains are crystalline
239 solids susceptible to deformation by dislocation motion. For olivine, as an example, the dominant

240 plasticity mechanism at high stresses and low temperatures is found to be dislocation glide [King
241 and Marone, 2012]. As the temperature increases other mechanism may come into play such as
242 diffusion creep in diffusion of vacancies lead to dislocations climbing over pinning sites in the
243 lattice [King and Marone, 2012]. Eventually, the local temperature will be high enough to melt
244 some of the minerals in the grains leading to a significant drop in the contact frictional strength
245 [Rice, 2006].

246

247 To model dislocation glide, we follow Goetze [1978] and adopt the following formulation for the
248 flow strength at the grain contacts:

249

$$250 \quad s_{th} = \sigma_p \left[1 - \left(\frac{-RT}{\Delta H} \ln \frac{\dot{\gamma}}{B} \right)^{1/q} \right], \quad (8)$$

251

252 where the Pirel's stress $\sigma_p = 8.5$ GPa, the gas constant $R = 8.314$ J/(mol K), the activation
253 enthalpy $H = 5.4 \times 10^5$ J/mol, the empirical constant $B = 5.7 \times 10^{11} \text{ s}^{-1}$, and the exponent q is taken
254 equal to 2.

255

256 At high slip rates, heat is generated at the contact surface faster than it can diffuse. It follows that
257 the local temperature increases and may be high enough to generate a thin layer of molten
258 material at the contact surface or at least melt some of the minerals in the grain. This layer
259 lubricates the interface and reduces the local frictional strength to nearly zero. The occurrence of
260 this flash melting depends on the grain size, the porosity of granular layer, the background
261 temperature and the melting temperature of the grain constituents. There is also some evidence

262 that the strong degradation in the asperity strength may start at temperatures slightly lower than
 263 the overall melting point of the grain contact due to the melting of some of its minerals [Rice,
 264 1999; Tullis and Goldsby, 2003; Rice, 2006; Beeler et al., 2008]. For this purpose, we assume
 265 the following empirical formula that connects the low temperature plastic strength of the asperity
 266 with the high temperature flow strength:

$$267 \quad s_{th} = \sigma_p \left[1 - \left(\frac{-RT}{\Delta H} \ln \frac{\dot{\gamma}}{B} \right)^{1/q} \right] f(T, T_w), \quad (9)$$

268 where T_w is the characteristic weakening temperature of the grain mineral, and T is the local
 269 contact temperature. It is given by $T = T_b + \Delta T$, where T_b is the background temperature and
 270 ΔT is the local rise in temperature.

271 The function $f(T, T_w)$ is proposed to capture the degradation of the asperity contact strength at
 272 elevated temperature. We assume that $f(T, T_w) = 1$ for $T < T_w$. In this limit, Eqn. (9) coincides
 273 with Eqn. (8). On the other hand, for $T \gg T_w$, the strength function $f(T, T_w)$ should
 274 asymptotically approach zero. The rate of strength degradation depends on many factors such as
 275 the chemical environment, the grain metallurgy and the melting characteristics of the grain
 276 constituents. The specific form of $f(T, T_w)$ may be constrained from experiments or numerical
 277 simulations as we will discuss in Section VI. We emphasize, however, that T in Eqn. (9) is the
 278 total temperature at the grain contact which is the sum of the background temperature and the
 279 rise in temperature due to the flash heating processes. It follows from Eqns. (7) and (9) that the
 280 minimum flow stress s_o is given by:

$$s_o = \sigma_p \frac{s_c}{H} \left[1 - \left(\frac{-RT}{\Delta H} \ln \frac{\dot{\gamma}}{B} \right)^{1/q} \right] f(T, T_w). \quad (10)$$

Several models were proposed to describe viscoplasticity in crystalline materials. These include the simple Arrhenius-based activation model [Chester, 1994; Nakatani, 2001; Rice et al., 2001; Noda, 2008]; the Steinberg-Cochran-Guinan-Lund flow stress model [Steinberg et al., 1980], the mechanical threshold stress flow model [Follansbe and Kocks, 1988] and Preston-Tonks-Wallace flow stress model [Preston et al., 2003]. In these last three models, the flow stress is expressed as a sum of two terms: an athermal component and thermal one. The thermal component of the flow stress is the product of two terms. The first one is the component of the flow stress due to thermally activated processes (e.g. dislocation motion). The second term takes the form $\mu(p, T)/\mu_o$ where $\mu(p, T)$ is the pressure and temperature dependent shear modulus and μ_o is a reference shear modulus. Equations (9) and (10) have a similar construction. There, the thermally activated component of the flow stress is given by the dislocation creep model (Eqn. (8)). Accordingly, we hypothesize that the function $f(T, T_w)$ may be reflecting thermal variation in the shear modulus of the region in the vicinity of the grain contacts. Constructing the function $f(T, T_w)$ from first principles is beyond the scope of this paper but we give an example for a plausible form in Section VI.

IV. Single Contact Temperature Model

We assume that all contacts are initially at the background temperature T_b . The increase in temperature due to local shear heating at the grain contact is computed as follows. The heat generation rate per unit area during sliding is given by $s_l V = sA/A_r V^* = sH/s_c V^*$, where V^* is the local slip rate. This heat source is assumed to be confined to the plane of contact. By convolving

302 the fundamental solution of the heat diffusion equation with this planar heat source [Appendix
 303 A], the temperature rise at the interface is given by:

$$304 \quad \Delta T = \frac{1}{2\rho c\sqrt{\pi\alpha_{th}}} \int_t^{t+\Delta t} \frac{s(t')V^*(t')}{\sqrt{t-t'}} \frac{H}{s_c} dt' \quad . \quad (11)$$

305 The absolute temperature of the contact is then given by

$$306 \quad T = T_b + \Delta T \quad . \quad (12)$$

307 When the heat generation rate is constant, the maximum temperature rise occurs at the end of the
 308 contact lifetime, i.e. at $\Delta t = a/V^*$ where a is the grain size. This maximum rise is given by:

$$309 \quad \Delta T_{\max} = \frac{sV^*H}{2s_c\rho c\sqrt{\pi\alpha_{th}}} \sqrt{a/V^*} = \frac{sH}{2s_c\rho c} \frac{\sqrt{aV^*}}{\sqrt{\pi\alpha_{th}}} \quad . \quad (13)$$

310 For general time-dependent heat sources, Eqn. (11) is integrated numerically. If the slip rate at
 311 the grain contact is not constant, the contact time is defined implicitly through the integral

$$312 \quad \int_t^{t+\Delta t_c} V^* dt = a \quad . \quad (14)$$

313 **V. Assembly of Contacts**

314 As the gouge layer is sheared, many grains are actively sliding past one another. These grain
 315 contacts are at different stages in their slip history; while two grains may be at the end of their
 316 contact lifetime, another pair may be just starting the process (Fig. 3). In the one dimensional
 317 idealization, adopted here, all STZs are arranged in series with respect to the direction of shear
 318 stress. That is, the macroscopic plastic strain rate is the sum of the individual microscopic plastic
 319 strain rates of the STZs. The shear stress for all STZs is the same, however. This is analogous to

320 a chain of grains that is sheared at one end. This has two implications. First, the slip rate at the
321 grain contact is not, in general, equal to the imposed slip rate. Compatibility of macroscopic and
322 microscopic deformations dictates that $N\Lambda V^* = \dot{\gamma}h = V$, or equivalently:

$$323 \quad V^* = \dot{\gamma}a/\Lambda . \quad (15)$$

324 Here, we made the assumptions that all grain contacts slide at the same rate V_{stz} . Furthermore, we
325 have let $a = h/N$. Second, the minimum flow stress in the system s_o is controlled by the sliding
326 site with the highest temperature, or equivalently, the lowest strength. This latter conclusion
327 follows from the chain analogy; under uniform stress a chain breaks at its weakest link.
328 Equations (15) and (13) imply that the rise in temperature for gouge particles depends not only
329 on the grain size but also on the degree of disorder in the system, as given by Λ^{eq} . This is an
330 important difference between sliding on a rock surface and sliding by shearing a gouge layer.

331 **VI. Parameter Selection**

332 Two sets of parameters are used in the current model. The first set relates to the parameters of
333 the STZ theory. The other set is related to the thermal properties of the gouge particles.

334 For the STZ parameters, we assume that the STZ strain ε_o is of the order of unity [Lieou and
335 Langer, 2012]. This corresponds to the assumption that during local rearrangements, a particle
336 will move a distance that is approximately equal to its size. The inertia time scale $\tau = a/(s_c/\rho)^{0.5}$,
337 where ρ is the grain density, is the time required for a particle to move a distance comparable to
338 its size a under the influence of pressure s_c [da Cruz et al., 2005; Lieou and Langer, 2012;
339 Lieou et al., 2014]. This time scale τ has been found to appropriately describe grain dynamics

340 for a wide range of slip rates. The inertia number $q = \dot{\gamma}\tau$ is the ratio of the plastic strain rate $\dot{\gamma}$ to
341 the strain rate associated with the inertial motion $1/\tau$. In applications relevant to seismology,
342 the pressure may be as large as a few hundred MPa. We take s_c in the subsequent calculations to
343 be equal to 75 MPa unless otherwise stated. The critical inertia number q_o , at which the disorder
344 temperature diverges and the inertial flow commences, is assumed to be 0.1-1 [da Cruz et al.,
345 2005; Roux J.-N. and Chevoir F, 2005; Job et al., 2006]. Previously [Langer and Manning,
346 2007.] it was shown that in the limit of small strain rates, the steady state value of the disorder
347 temperature approaches a constant value χ_o that is independent of strain rate. The specific value
348 depends on the nature of the system of particles (e.g. particle shapes and grain size distribution).
349 Numerical simulations of systems of hard spheres suggest that $\chi_o \approx 0.2$ [Haxton et al., 2011;
350 Lieou and Langer, 2012.]. In subsequent calculations, we vary χ_o between 0.15 and 0.30. Higher
351 values of χ_o correspond to less compacted states.

352 For the properties of the gouge particles, we assume the following nominal values: density
353 $\rho = 2700 \text{ kg/m}^3$, volumetric heat capacity $\rho c = 2.7 \times 10^6 \text{ J/m}^3\text{k}$, coefficient of thermal diffusivity
354 $\alpha_{th} = 10^{-6} \text{ m}^2/\text{s}$, and hardness $H = 6 \text{ GPa}$ [Rice, 2006; Noda, 2008]. These values weakly depend
355 on temperature.

356 **VII. Results**

357 To characterize the influence of local heating on the frictional response of the gouge layer, we
358 investigate both the steady state and transient behavior. We also examine the energy partitioning
359 between frictional heat and configurational work.

360 **VII.1. Steady state response**

361 If the gouge layer is sheared for a sufficiently long time under constant slip rate, steady state
 362 conditions will prevail. That is, no further evolution in the shear stress, plastic strain rate or
 363 disorder occurs. Mathematically, that is equivalent to setting $\dot{\gamma} = V/h$, $\chi = \hat{\chi}$ and $s = s_{ss}$ in Eqn.
 364 (1). The minimum flow stress s_o is calculated based on Eqn. (10) with $T_{ss} = T_b + \Delta T_{ss}$ (Eqn.
 365 (12)) where ΔT_{ss} is the rise in contact temperature at steady state due to local heating. This latter
 366 quantity can be estimated from Eqn. (13) by setting $V^* = V_{stz} = \frac{\dot{\gamma}a}{\Lambda} = \frac{V}{h} a \exp(1/\hat{\chi})$. It follows that:

$$367 \quad \Delta T_{ss} = \frac{sHa}{2s_c \rho c} \sqrt{\frac{\exp(1/\hat{\chi})}{\pi \alpha_{th} h}} \sqrt{V} \quad . \quad (16)$$

368 Here we have made use of the relation $\Lambda = \exp(-1/\chi)$. The steady state shear stress is then
 369 determined by solving the following equation simultaneously with Eqn. (16)

$$370 \quad \frac{V}{h} = (\varepsilon_o/\tau_o) \left(1 - \frac{s_o(T_{ss})}{s_{ss}} \right) \exp\left(\frac{s_{ss}}{s_c \hat{\chi}} \right) \exp(-1/\hat{\chi}). \quad (17)$$

371 The minimum flow stress s_o is calculated using Eqn. (10), and the form of $f(T, T_w)$ is
 372 constrained by experimental measurements.

373 As an example, we consider the series of high speed frictional experiments of Sone and
 374 Shimaoto [2009]. In these experiments, a layer of fault gouge 1mm thick is sheared at different
 375 slip rates in the range of 0.1-2.1 m/s under 0.56 MPa normal stress. They reported that the steady
 376 state shear stress varies exponentially with the imposed slip rate. This is represented by the
 377 discrete points in Fig. 4.

378 To fit the experimental observations, we solve Eqns. (10), (16) and (17). For this purpose, we
 379 make the simplified assumption that the steady state effective temperature is constant and
 380 independent of strain rate, i.e. $\hat{\chi} = \chi_o$. This may be justified as follows. The fluidizing strain
 381 rate $\dot{\gamma}_c$ corresponding to the experimental conditions discussed here is given by q_o/τ where
 382 $q_o = 1$ and $\tau = a/\sqrt{s_c/\rho} = 6.94 \times 10^{-7} s$ (assuming average grain size $a = 10 \mu m$). This yields
 383 $\dot{\gamma}_c = 1.44 \times 10^6 s^{-1}$ which is almost three orders of magnitude larger than the highest macroscopic
 384 strain rate reported in the experiment ($2100 s^{-1}$). For strain rates that are much lower than the
 385 fluidizing strain rates, previous work [Langer and Manning, 2007] suggests that the steady state
 386 effective temperature is well approximated by its low strain rate limit. We adopt this
 387 simplification here and assume $\chi_o = 0.15$. The weakening temperature T_w varies depending on
 388 the material composition of the grains. It ranges from $750^\circ C$ for biotite [Rice, 2006] to
 389 approximately $1200^\circ C$ for silicates. Here, we choose $T_w = 1300 K$.

390 For low strain rates, the increase in contact temperature is miniscule (a few degrees) [Mair and
 391 Marone, 2000; Mair et al., 2006]. In this limit, our theory predicts that the steady state response
 392 is rate strengthening (Fig. 3). In Section II we showed that STZ theory predicts rate independent
 393 behavior for sheared granular material at low strain rates, and this prediction is consistent with
 394 numerical simulation of soft and hard spheres [e.g. da Cruz et al., 2005]. The rate strengthening
 395 response shown here has been reported in frictional experiments on fault gouge [e.g. Chester
 396 1994; Blanpied et al., 1995] and has been explained within the framework of rate and state
 397 friction [Dieterich, 1979; Ruina, 1980] which was developed primarily for sliding on rock
 398 surfaces. We attribute this behavior to the rate dependence of the contact strength (Eqn. (8)) that
 399 overtakes the weakening effect due to temperature changes. Figure (4) suggests that for slip rates

400 smaller than 1mm/s the steady state friction coefficient depends logarithmically on the slip rate
 401 and that $\partial\mu_{ss}/\partial\log V = 0.0075$. Similar values have been documented experimentally [Dieterich,
 402 1979; Ruina, 1980; Chester, 1994; Blanpied et al., 1995; Marone, 1997].

403 To match the behavior at high strain rates, corresponding to $V > 0.1$ m/s, the functional form of
 404 $f(T, T_w)$ must be determined. We found the following form to yield the best results:

$$405 \quad f(T, T_w) = C \exp\left(-r\left(\frac{T - T_b}{T_w - T_b}\right)^2\right), \quad (18)$$

406 where $T_b = 300$ K, $r = 2$ and $C = \exp(r)$. Expanding the exponential function in Eqn. (18) and
 407 defining $T_* = (T - T_b)/(T_w - T_b)$ we obtain the following approximation:

$$408 \quad f \approx 1 - rT_*^2, \quad (19)$$

409 In this limit, we recover the temperature-dependent term in the Johnson-Cook flow stress model
 410 with $m = 2$ [Johnson and Cook, 1983]. This approximation is valid for T in the vicinity of T_w .

411 The predictions of the model fit the experimental measurements very well for slip rates ranging
 412 between 0.1 m/s and 1.25 m/s. For higher slip rates, the friction coefficients reported
 413 experimentally are lower than what the model predicts. We hypothesize that this discrepancy
 414 may be attributed to strain localization which is enhanced at higher slip rates. In the current
 415 model, the strain rates are computed assuming a shear zone thickness of 1mm. Sone and
 416 Shimamoto [2009] observed that the strain may localize to bands 100-150 μm thick. The strain
 417 rate in the shear band is usually higher than the average strain rate [Manning et al., 2007]. The
 418 shear band thickness broadens with time [Manning et al., 2007; Lieou et al., 2014], nonetheless,

419 and its dynamics depend on the imposed strain rate. We expect strain localization to be enhanced
420 at higher slip rates. This in turn leads to larger increases in local temperature and lower flow
421 strength. Thus, we conjecture that modeling strain localization will result in a better quantitative
422 fit for the data at higher slip rates. This will be the subject of a future investigation.

423 **VII.2. Transient Response**

424 To examine the full response of the sheared gouge layer, including direct and evolution effects,
425 we integrate the STZ equations of motion, Eqns. (1) and (3), coupled with the equation for
426 contact temperature (Eqn. (11)). To complete the dynamical description of the system, we
427 augment the STZ equations by an equation for the evolution of the shear stress:

$$428 \quad \dot{s} = G \left(\frac{V}{h} - \dot{\gamma} \right), \quad (20)$$

429 Where G is the shear stiffness of the system per unit length and V/h is the imposed strain rate.
430 We assume $G = 30$ GPa and consider high strain rates in the range of 10^3 to $10^4 s^{-1}$. We assume
431 $s_c = 75$ MPa, $a = 1$ μm , $T_b = 273$ K, $T_w = 1000$ K, and $\chi_o = 0.27$. These values lead to reasonable
432 computational cost and are within the range of physically plausible limits for fault gouge. All
433 other parameters are taken as in the previous sections.

434 **VII.2.1. Velocity stepping experiment**

435 Figures 5a shows the result for a pair of velocity stepping numerical experiments between strain
436 rates 10^3 and $2 \times 10^3 s^{-1}$. The inserts expand the scales to visualize the shear stress variations
437 right after the upward and downward velocity steps. Several remarks follow from this figure.
438 First, the response is asymmetric for the upward and downward steps. The downward direct
439 effect is slightly larger with a magnitude of 0.154 MPa whereas the magnitude of the upward

440 direct effect is 0.144 MPa. Second, the evolution of friction following the downward step is
441 steeper than the one following the upward step. Third, following a mathematical step in imposed
442 slip rate, the frictional stress does not follow with an infinite slope as predicted for bare rock
443 surfaces in contact [Noda, 2008]. Rather, it gradually evolves, especially in the downward
444 velocity step case.

445 The previous observations continue to hold for larger changes in strain rates. Figure (5b) shows
446 the results for a velocity stepping numerical experiment between 10^3 and $10^4 s^{-1}$. The upward
447 direct effect is equal to 0.5 MPa while the downward direct effect is equal to 0.64 MPa,
448 compared to 0.144 MPa and 0.154 MPa in the smaller step magnitude experiments, respectively.

449 These results suggest that the normalized direct effect, $\partial s / \partial (s_c \log(V_2/V_1))$, increases with the
450 magnitude ratio of the velocity step V_2/V_1 .

451 The asymmetry between the upward and downward direct effect, which increases as the
452 magnitude of the strain rate step increases, may be explained by the thermo-mechanical coupling
453 in our model. As the system is sheared, grains come into and out of contact continuously.
454 Following a velocity step, regardless of its direction, the contact temperature will initially
455 increase. We show in Figs (5c) and (5d) an example for the temperature evolution corresponding
456 to the stress-strain curve in Fig. (5a). In case of an upward velocity step, the contact temperature
457 continues to rise (Fig. 5c). For a downward velocity step, however, the contact temperature will
458 reach a maximum and then decreases due to the reduced heat generation rate (Fig. 5d). This
459 difference in the evolution history of the contact temperature results in different evolution for s_o
460 and consequently different variation in the shear stress. A similar trend was observed in the
461 temperature variations corresponding to the stress-strain curve shown in Fig. (5b).

462

463

464 A common feature in Figs. 5a and 5b is that the evolution of stress as a function of strain,
465 following an upward step in velocity, is non-monotonic. The stress first decreases until it reaches
466 a minimum and then it increases again towards a steady state. This is explained by the evolution
467 of the local temperature at the grain contacts. Following an upward step in velocity, the contact
468 temperature first increases (see Fig. 5c for example). Diffusion effects become important as slip
469 accumulates. Accordingly, the temperature will reach a maximum and then gradually decreases
470 due to heat diffusion. This temperature trend causes the flow stress to first decrease and then
471 increase. The shear stress follows the flow stress trend (Fig. 5a).

472 **VII.2.2 Velocity ramps experiment**

473 The high speed frictional experiments of Sone and Shimamoto [2009] were unique in their
474 ability to test the frictional response under decelerating and accelerating velocity ramps. Figure 6
475 shows the results of an analogous numerical experiment in which the imposed strain rate
476 increases linearly between 10^3 and $10^4 s^{-1}$ over a strain of 0.005 and then decreases again to
477 $10^3 s^{-1}$ over a strain of 0.015, after which it remains constant. In this case, it is observed that the
478 upward direct effect is reduced significantly compared to Fig. 6. During the upward velocity
479 ramp, the shear stress gradually decreases. The minimum shear stress value is comparable to the
480 minimum value in Fig. 5. However, it does not occur at the strain corresponding to the maximum
481 strain rate. The shear stress continues to decrease during a part of the downward velocity ramp.
482 This is attributed to the reduced value of the minimum flow stress that resulted from the increase
483 in temperature during the upward velocity ramp. Eventually, the shear stress starts to increase

484 while the imposed strain rate is decreasing. The cooling of the asperities due to the reduced heat
485 flux leads to an increase in s_o which in turn results in shear strengthening.

486 In Fig. 6b, we show experimental results from Sone and Shimamoto (2009) for a velocity
487 ramping experiment. In their experiment, a shear band of 100-150 μm was observed. Assuming
488 that the strain rate is totally accommodated by deformations within the band, a ramp in the
489 imposed slip rate between 0.1 and 1.0 m/s corresponds to a ramp in strain rates in the shear band
490 from 10^3 to 10^4 s^{-1} (assuming shear band thickness 100 μm). This is the range of strain rates we
491 tested numerically in Fig. 7a. The initial frictional strengthening observed experimentally is due
492 to starting the experiment from zero velocity which requires overcoming the “static friction” in
493 order for the plastic strain rate, and subsequent softening, to start to accumulate. In the numerical
494 model, however, the sample is sheared initially at 10^3 s^{-1} , and by the time the velocity ramp is
495 applied the system has significantly deformed. Another important difference between the
496 experiment and the numerical model is the pressure scale. The normal stress applied
497 experimentally is of the order of 0.56 MPa which is 150 times smaller than what is used in the
498 numerical simulations. This leads to experimentally longer evolution length and time scales.
499 Nonetheless, the model predictions and the experimental observations show good qualitative
500 agreement in the trend for stress evolution.

501 **VII.3. Energy partitioning**

502 In this section we quantify how the energy is partitioned in the gouge layer between its different
503 components. As the gouge layer is sheared, energy is dissipated as radiated energy, frictional
504 heat, and increases in local disorder. The total dissipation is given by:

$$505 \quad E_T = \int s(u) du . \quad (20)$$

506 The configurational energy E_c is the fraction of energy required to change the effective
 507 temperature and increase local disorder. The configurational energy per unit area is given by:

$$508 \quad E_c = h \int c_o s_c d\chi = \int [hc_o s_c d\chi/du] du. \quad (21)$$

509 In this paper we do not consider inertial effects or energy lost to radiation. We thus attribute the
 510 remaining dissipation to thermal heating. The heat dissipated per unit area E_f is the difference
 511 between the total and configurational energy per unit area,

$$512 \quad E_f = E_T - E_c = \int [s(u) - hc_o s_c d\chi/du] du. \quad (22)$$

513 An example of the partitioning between these two modes of energy dissipation is shown in Fig.
 514 8. The amount of energy dissipated per unit area as frictional heat and configurational energy are
 515 represented by the yellow and red areas respectively. The upper curve in both figures represents
 516 the actual shear stress in the system. The boundary between the red and the yellow regions
 517 represents the frictional heat stress s_f . This is defined as fraction of shear stress contributing to
 518 heat generation. From Eqn. [22] this fraction is given by:

$$519 \quad s_f = s(u) - hc_o s_c d\chi/du. \quad (23)$$

520 We can immediately see from Fig. 7 that configurational energy is not be a negligible part of the
 521 energy budget. In this particular case, nearly 10% of the dissipated energy is consumed in
 522 increasing local disorder. This percentage varies depending on pressure, the initial value of the
 523 effective temperature (which reflects how loose or compact the sample initially is), the value of
 524 steady state effective temperature, and the magnitude of slip. If the system is sheared long

525 enough to reach configurational steady state, there will be no further increase in the local
526 disorder and the configurational energy will diminish. In that limit, all work as dissipates as heat.

527 **VIII. Discussion**

528 Earthquakes are frictional instabilities which occur because fault strength weakens with
529 increasing slip or slip rate [Rice, 2006]. Field observations suggest that slip in individual events
530 on mature faults occurs primarily within a thin shear zone, <1–5 mm, that occurs inside a finely
531 granulated fault zone [Chester and Chester, 1994]. In absence of a strong weakening mechanism,
532 temperature rise would lead to widespread melting. Nonetheless most exhumed faults shows a
533 lack of evidence for the existence of pseudotachylyte that would be left from rapid recooling of
534 the molten rocks. Relevant weakening processes in crustal events are likely to be activated by
535 thermal processes during dynamic slip. Several processes have been proposed such as (1)
536 thermal pressurization of pore fluids, and (2) flash melting at highly stressed frictional
537 microcontacts [Rice, 2006]. In this paper, we implement temperature-dependent viscoplasticity
538 and the theory of flash heating within the framework of Shear transformation Zone (STZ) theory
539 to predict the frictional response of sheared gouge layers at different slip rates and confining
540 normal stresses.

541 Important differences exist between sliding on bare rock surfaces and shearing a layer of
542 granular materials. Mainly, granular particles possess extra degrees of freedom compared to
543 asperities on rock surfaces. Grains have both translational and rotational degrees of freedom and
544 the plastic strain rate is partitioned between these different modes. This further enables grains to
545 rearrange and to accumulate plastic deformation through this process. This flexibility is not
546 available for rock asperities.

547 For rock surfaces sliding past one another, the asperities on the contact surfaces are arranged in
548 parallel with the shear force. As a result, it is natural to assume that (1) the slip rate at all active
549 asperities is equal to the imposed slip rate, and (2) the applied shear force is the sum of the local
550 shear forces at the asperities. It follows that the strength of the interface is the summed resistance
551 of all contacts and is not governed by the weakest one. In this case, the strength is determined by
552 the average contact temperature and not the maximum temperature [Noda, 2008].

553 In sheared granular materials the opposite situation occurs. STZs are arranged in series with the
554 shearing force, analogous to a chain of beads that is loaded at one end (Fig. 3). The shear stress
555 may be assumed to be constant across the granular layer so that all STZs are subject to the same
556 stress. The imposed slip rate, however, is partitioned among the active STZs. Accordingly, the
557 local slip rate at an STZ site may be significantly different from the imposed slip rate depending
558 on the STZ density. The larger the number of STZs the smaller the local slip rate compared to
559 the imposed slip rate. Another consequence is that the strength of the system is governed by the
560 strength of the “weakest” STZ. Using the chain analogy and under uniform stress, the strength of
561 the chain is governed by its weakest link. In the context of the current paper, the weakest link
562 corresponds to the sliding site with the smallest local friction or the highest contact temperature.

563 Other theories for temperature dependent weakening mechanisms in gouge have been proposed
564 earlier. Chester (1994) proposed a state-variable constitutive relation, within Dieterich-Ruina rate
565 and state friction framework, which describes the dependence of friction on temperature near
566 steady state conditions. Their approach is suitable for very low slip rates ($\mu\text{m/s}$) and is based on
567 the assumption that the micromechanisms of friction are thermally activated and follow an
568 Arrhenius relationship. Here, we consider the general umbrella of viscoplastic processes that
569 may occur at the grain contacts at different temperatures and slip rates. By incorporating

570 viscoplasticity with the STZ theory, which takes into account the amorphous nature of the
571 granular layer, we connect the local processes at the grain contacts with the macroscopic plastic
572 strain accumulated by particles slip and rearrangement. The relevant temperature for the
573 activation of the viscoplastic processes is the absolute local temperature at the grain contact. This
574 is the sum of the background macroscopic temperature and the local temperature rise due to flash
575 heating processes. We were able to numerically calculate the changes in temperature at the grain
576 level for different slip rates and to quantify the interaction between thermally activated
577 viscoplasticity and granular dynamics. We showed that this interaction may lead to a non-
578 monotonic granular rheology. Incorporating these thermally activated processes within the STZ
579 framework will allow us to explore the effect of temperature changes on processes like shear
580 banding which are not directly resolved by the other approaches.

581 In this paper, we assumed that the background temperature is kept constant by continuous
582 cooling. In real faults, this condition is not satisfied in general. Sliding for long distances will
583 inevitably cause an increase in the macroscopic temperature. This will require solving the heat
584 diffusion equation for the background temperature with the heat source term corresponding to
585 the macroscopic heat generation rate $s\dot{\gamma}$. In this case the absolute temperature at the grain
586 contact is calculated by adding the local rise in temperature to the evolving background
587 temperature. The higher the background temperature, the smaller the increase in local
588 temperature required to initiate strong rate weakening. We thus expect that modeling the changes
589 in macroscopic temperature will modify the slip rate at which significant weakening is observed.

590 The form of the flow rule used here to describe dislocation glide was developed specifically for
591 Olivine [Goetze, 1978]. It may be regarded as a special case of the more generalized mechanical
592 stress threshold flow model [Follansbe and Kocks, 1983]. At low slip rates, the adopted flow rule

593 predicts changes in frictional strength similar to those observed experimentally (See Fig. 3). At
594 high slip rates, the influence of the thermally activated part of the flow rule diminishes as the
595 strength is controlled more by the flash heating processes and the function $f(T, T_w)$. We expect
596 qualitatively similar behavior to be obtained if a simplified Arrhenius relationship [Chester,
597 1994; Noda, 2008] is used for the flow rule. The advantage of the mechanical stress threshold
598 model is that it is more flexible and enables the inclusion of microstructure damage evolution at
599 the asperity level. This is relevant for further improvement in the theory.

600 Granular dynamics is usually described as rate insensitive at low strain rates and rate
601 strengthening at high strain rates. This has been reported in numerous numerical and
602 experimental observations [e.g. da Cruz et al., 2005]. Fault gouge, however, exhibit viscoplastic
603 properties and was shown experimentally to exhibit both rate strengthening and rate weakening
604 response [Chester, 1994; Blanpied et al., 1995; Sone and Shimamoto, 2009]. Our modified
605 version of STZ theory with temperature-dependent viscoplastic interactions predicts a modest
606 rate strengthening at low strain rates. At high strain rates, the contact temperature rises
607 significantly. This leads to strong rate weakening that mimicks the exponential degradation in
608 strength reported in Sone and Shimamoto [2009].

609 In shearing dry granular layers, dissipated energy is partitioned between frictional heat and
610 configurational energy. The former is responsible for increasing the layer temperature while the
611 latter facilitates local disorder [Hermundstadt et al., 2010]. Thermal weakening reduces the total
612 amount of dissipated energy compared to cases when the strength is modeled as a temperature
613 independent property by reducing the value of the sliding stress at any given strain. Moreover,
614 we have shown that a portion of the total energy, estimated here to be of the order of 10%, is

615 expended in increasing local disorder. This further reduces the amount of energy dissipated by
616 heat.

617 Depending on the strain rate and grain size distribution, strain may localize to a band that is less
618 than 1mm thick [Sone and Shimamoto, 2009]. Shear banding is as an additional weakening
619 mechanism that affects both the level of the sliding shear stress and the slip weakening distance.
620 STZ theory provides a powerful tool for resolving strain localization at different strain rates
621 [Daub et al., 2008; Manning et al., 2009; Hermundstad et al., 2010]. We expect thermal
622 weakening to enhance the localization process and to affect the dynamics of growth of the shear
623 band.

624 In continuum systems, a fraction of total energy is dissipated as radiated energy. This additional
625 energy sink was not considered in this paper. We expect systems which weaken rapidly, as a
626 result of thermal weakening, to radiate more energy for the same amount of slip. This in turn will
627 affect the resulting ground motion and in particular its high frequency content..

628 Seismic inversions in a number of events, such as the Tohoku earthquake [Mori, 2011; Romano
629 et al., 2012], suggest that dynamic rupture propagated for significant distances in what had been
630 identified as rate strengthening regions. Here we considered a rate strengthening granular
631 material as a basic model but showed that thermal weakening, due to local heating of grain
632 contacts, may provide a mechanism by which a material, that is rate strengthening at low slip
633 rates, significantly weakens at high slip rates. This implies that rate strengthening regions may
634 not always impede rupture propagation. Accordingly, on a fault with both rate strengthening and
635 rate weakening regions, limiting the expected maximum size of an earthquake to the length of

636 the rate weakening zone only could be a dangerous underestimation with serious implications for
637 seismic hazard.

638 A controlling parameter for the strength of gouge particles with viscoplastic properties is the
639 maximum increase in temperature at the grain contact. The theoretical formulation presented in
640 this paper suggest that this maximum temperature does not depend only on the grain size but also
641 on the state of disorder of the system (see, e.g., Eqn. 16). Compacted systems are more
642 susceptible to higher increases in temperature. This dependence on the degree of disorder, or the
643 way of sample preparation in terms of looseness or compactness, has no analogy in the case of
644 sliding on bare rock surfaces and is an important characteristic of granular systems

645 As the material is sheared, two competing mechanisms control the temperature variations; the
646 rate of heat generation and the rate of thermal diffusion. For high slip rates, the former surpasses
647 the latter, and heat is localized, leading to temperature rise and reduction in contact strength. If
648 the slip rate decreases, the effect of thermal diffusion will eventually dominate leading to a
649 reduction in the temperature. This increases the contact strength and leads to re-strengthening.
650 Hence, the temperature dependence of the contact strength allows for both rapid weakening and
651 healing of the sheared gouge layer. This provides a framework for the analysis of constitutive
652 response for different loading rate scenarios, including velocity stepping and ramping
653 experiments, as discussed here, as well as slide-hold-slide tests. In particular, accounting for
654 flash processes at grain contacts may be an important ingredient in understanding the difference
655 in healing rates following low and high speed frictional experiments.

656

657

658 **Acknowledgements**

659 The authors wish to thank James Langer, and Ralph Archuleta for the helpful discussions. A.E.
660 Elbanna is grateful for H. Sone and H. Shimamoto for sharing their data and insights into the
661 experimental implications. This research was funded by NSF/USGS Southern California
662 Earthquake Center, funded by NSF 489 Cooperative Agreement EAR0529922 and USGS
663 Cooperative Agreement 07HQAG0008, and by Office of Naval Research MURI grants
664 N000140810747 (<http://www07.grants.gov/search/search.do?oppId=42747&mode=VIEW>)
665 and 0001408WR20242.

666

667

668

669

670

671

672

673

674

675

676

677

678

679

680

681

682 **References**

683 Aagaard, B., and T. Heaton (2008), Constraining fault constitutive behavior with slip
684 heterogeneity, *J. Geophys. Res.*, VOL. 113, B04301, doi:10.1029/2006JB004793.

685

686 Ampuero J. P. and Y. Ben-Zion (2008), Cracks, pulses and macroscopic asymmetry of dynamic
687 rupture on a bimaterial interface with velocity-weakening friction, *Geophys. J. Int.*, 173 (2), 674-
688 692, doi:10.1111/j.1365-246X.2008.03736.x

689

690 Beeler, N. M., T. E. Tullis, and D. L. Goldsby (2008), Constitutive relationships and physical
691 basis of fault strength due to flash heating, *J. Geophys. Res.*, 113, B01401,
692 doi:10.1029/2007JB004988.

693

694 Ben-Zion, Y., and C. G. Sammis (2003), Characterization of fault zones, *Pure Appl. Geophys.*,
695 160, 677–715.

696 Blanpied, M., Lockner, D. and Byerlee, J. (1995). Frictional slip of granite at hydrothermal
697 conditions. *Journal of Geophysical Research* 100: doi: 10.1029/95JB00862. issn: 0148-0227.

698 Bouchbinder, E and J.S. Langer (2009c), “Nonequilibrium thermodynamics of driven amorphous
699 materials. III. Shear-transformation-zone plasticity,” *Phys. Rev. E* 80, 031133,
700 10.1103/PhysRevE.80.031133.

701 Brune, J. N., T. L. Henyey, and R. F. Roy (1967), Heat flow, stress, and rate of slip along the San
702 Andreas Fault, California, *J. Geophys. Res.*, 74(15), 3821–3827.

703 Chester, F. M. (1994), Effects of temperature on friction: Constitutive equations and experiments
704 with quartz gouge, *J. Geophys. Res.*, 99(B4), 7247–7261, doi:10.1029/93JB03110.

705 Chester, F. M., and J. S. Chester (1998), Ultracataclasite structure and friction processes of the
706 Punchbowl Fault, San Andreas system, California, *Tectonophysics*, 295, 199–221.

707 Chester, F. M., J. P. Evans, and R. L. Biegel (1993), Internal structure and weakening
708 mechanisms of the San Andreas fault, *J. Geophys. Res.*, 98, 771–786.

709

710 Chester, F. M., J. S. Chester, D. L. Kirschner, S. E. Schulz, and J. P. Evans (2004), Structure of
711 large-displacement, strike-slip fault zones in the brittle continental crust, in *Rheology and*
712 *Deformation in the Lithosphere at Continental Margins*, edited by G. D. Karner et al., pp. 223 –
713 260, Columbia Univ. Press, New York.

714

715 da Cruz, F., S. Emam, M. Prochnow, J. N. Roux, and F. Chevoir (2005), Rheophysics of dense
716 granular materials: Discrete simulation of plane shear flows, *Phys. Rev. E*, 72, 021309,
717 doi:10.1103/Phys-RevE.72.021309.

718

719 Daub, E. G., and J. M. Carlson (2008), A constitutive model for fault gouge deformation in
720 dynamic rupture simulations, *J. Geophys. Res.*, 113, B12309, doi:10.1029/2007JB005377.

721 Daub, E. G., M. L. Manning, and J. M. Carlson (2008), Shear strain localization in elastodynamic
722 rupture simulations, *Geophys. Res. Lett.*, 35, L12310, doi:10.1029/2008GL033835.

723 Dieterich, J. H. (1979), Modeling of rock friction 1. Experimental results and constitutive
724 equations, *J. Geophys. Res.*, 84(B5), 2161–2168.

725 Follansbee, P.S.; Kocks, U.F. (1988), "A constitutive description of the deformation of copper
726 based on the use of the mechanical threshold", *Acta Metallurgica* 36 (1): 81–93,
727 doi:10.1016/0001-6160(88)90030-2.

728 Falk, M. L., and J. S. Langer (1998), Dynamics of viscoplastic deformation in amorphous solids,
729 *Phys. Rev. E*, 57(6), 7192–7205.

730 Falk, M. L., and J. S. Langer (2000), From simulation to theory in the physics of deformation
731 and fracture, *MRS Bull.*, 25(5), 40–45.

732 Goetze, C. (1978), Mechanisms of creep in olivine, *Philos. Trans. R. Soc. London, Ser. A*, 288,
733 99–119.

734 Haxton, T. K., and A. J. Liu (2007), Activated dynamics and effective temperature in a steady
735 state sheared glass, *Phys. Rev. Lett.*, 99, 195701.

736 Heaton, T. H. (1990), Evidence for and implications of self-healing pulses of slip in earthquake
737 rupture, *Phys. Earth. Planet. Inter.*, 64, 1– 20.

738 Hermundstad, A., Daub, E. G., and J. M. Carlson (2010), "Energetics of strain localization in a
739 model of seismic slip," *J. Geophys. Res.*, Vol 115, B06320, doi:10.1029/2009JB006960.

740

741 Johnson, G.R.; Cook, W.H. (1983), "A constitutive model and data for metals subjected to large
742 strains, high strain rates and high", *Proceedings of the 7th International Symposium on Ballistics*:
743 541–547.

744

745 Jop, P., Y. Forterre, and O. Pouliquen (2006), A constitutive law for dense granular flows,
746 Nature, 441(8), 727–730.

747 King, D. S. H. and C. Marone, Frictional properties of olivine at high temperature with
748 applications to the strength and dynamics of the oceanic lithosphere, J. Geophys. Res., 117,
749 B12203, 10.1029/2012JB009511, 2012.

750 Kanamori, H., and T. H. Heaton (2000), Microscopic and macroscopic physics of earthquakes, in
751 Geocomplexity and the Physics of Earthquakes, American Geophysical Union Geophysical
752 Monograph 120, pp. 147–163, AGU, Washington, D. C.

753 Lachenbruch, A. H. (1980), “Frictional heating, fluid pressure, and the resistance to fault
754 motion,” *J. Geophys. Res.* 85 (B11), 6097-6112.

755

756 Langer, J. S.,(2004), "Dynamics of shear-transformation zones in amorphous plasticity:
757 Formulation in terms of an effective disorder temperature," *Phys. Rev. E* 70, 041502,
758

759 Langer, J. S. (2008), Shear-transformation-zone theory of plastic deformation near the glass
760 transition, *Phys. Rev. E*, 77, 021502.

761 Langer, J. S., and M. L. Manning (2008), Steady-state, effective-temperature dynamics in a
762 glassy material, *Phys. Rev. E*, 76, 056107.

763 Lapusta, N., and J. R. Rice (2003), Low-heat and low-stress fault operation in earthquake models
764 of statically strong but dynamically weak faults, *Eos Trans. AGU*, 84(46), Fall Meet. Suppl.,
765 Abstract S51B-02.

766 Lemaitre, A., and J. M. Carlson (2004), Boundary lubrication with a glassy interface, *Phys. Rev.*
767 *E*, 69(6), 061611.

768 Lieou, C. K. C. and J. S. Langer (2012), “Dynamics of sheared hard spheres based on Edward's
769 statistical mechanics and the shear-transformation-zone theory”, *Phys. Rev. E* 85
770

771 Lieou, C. K. C., Elbanna, A. E. and J. M. Carlson (2014), “Grain fragmentation in sheared
772 granular flow: weakening effects, energy dissipation, and strain localization”, *Phys. Rev. E* (*to*
773 *appear*) <http://arxiv.org/abs/1311.3288>
774

775 Lockner, D., H. Naka, H. Tanaka, H. Ito, and R. Ikeda (2000), Permeability and strength of core
776 samples from the Nojima fault of the 1995 Kobe earthquake, in *Proceedings of the International*
777 *Workshop on the Nojima Fault Core and Borehole Data Analysis*, Tsukuba, Japan, Nov 22– 23
778 (1999), edited by H. Ito et al., U. S. Geol. Surv. Open File Rep., 00-129,147– 152.
779

780 Mair, K., and C. Marone (2000), “Shear heating in granular layers,” *Pure Appl. Geophys.* 157,
781 1847-1866, 10.1007/PL00001064.
782

783 Mair, K., F. Renard, and O. Gunderson (2006), Thermal imaging on simulated faults during
784 frictional sliding, *Geophys. Res. Lett.*, 33, L19301, doi:10.1029/2006GL027143.

785 Manning, M. L., Daub E. G., Langer J. S., and Carlson J. M., “Rate-dependent shear bands in a
786 shear-transformation-zone model of amorphous solids,” *Phys. Rev. E*, 79:016110, (2009),
787 10.1103/PhysRevE.79.016110
788

789 Manning, M. L., J. S. Langer, and J. M. Carlson (2007), Strain localization in a shear
790 transformation zone model for amorphous solids, *Phys. Rev. E*, 76(5), 056106.

791 Marone, C. (1998), Laboratory-derived friction laws and their application to seismic faulting,
792 *Ann. Rev. Earth Planet. Sci.*, 26, 643–696.

793 Nakatani, M. (2001), Conceptual and physical clarification of rate and state friction: Frictional
794 sliding as a thermally activated rheology, *J. Geophys. Res.*, 106(B7), 13347–13380,

795 Noda, H., and T. Shimamoto (2005), Thermal pressurization and slip-weakening distance of a
796 fault: An example of the Hanaore fault, southwest Japan, *Bull. Seismol. Soc. Am.*, 95(4), 1224 –
797 1233, doi:10.1785/0120040089.

798

799 H. Noda, E. M. Dunham and J. R. Rice (2009), "Earthquake ruptures with thermal weakening
800 and the operation of major faults at low overall stress levels", *Journal of Geophysical Research -*
801 *Solid Earth*, vol. 114, B07302, doi:10.1029/2008JB006143, 27 pages.

802

803 H. Noda, N. Lapusta and J. R. Rice (2011), "Earthquake sequence calculations with dynamic
804 weakening mechanisms", in *Multiscale and Multiphysics Processes in Geomechanics (results of*
805 *workshop at Stanford Univ., June, 2010)*, Springer Series in Geomechanics and Geoengineering,
806 edited by Ronaldo I. Borja, ISBN 978-3-642-19629-4, pp. 149-152.

807

808 Preston, D.L.; Tonks, D.L.; Wallace, D.C. (2003), "Model of plastic deformation for extreme
809 loading conditions", *Journal of Applied Physics* 93: 211, doi:10.1063/1.1524706.

810

811 Rice, J. R. (1980), The mechanics of earthquake rupture, in *Physics of the Earth's Interior*, edited
812 by A. M. Dziewonski and E. Boschi, 555–649, Elsevier, New York.

813

814 Rice, J. R. (2006), Heating and weakening of faults during earthquake slip, *J. Geophys. Res.*,
815 111, B05311, doi:10.1029/2005JB004006.

816 Romano, F., A. Piatanesi, S. Lorito, N. D'Agostino, K. Hirata, S. Atzori, Y. Yamazaki, and M.
817 Cocco (2012), Clues from joint inversion of tsunami and geodetic data of the 2011 Tohoku-oki
818 earthquake, *Nature: Scientific reports*, 2 : 385 | DOI: 10.1038/srep00385

819 Ruina, A. L. (1980), Friction laws and instabilities: A quasistatic analysis of some dry frictional
820 behavior, Ph.D. Thesis, Brown University, Providence,RI.

821 Scholz, C. H., “Earthquakes and friction laws,” *Nature* 391:37-42, (1998), 10.1038/34097
822

823 Scholz, C. H. (2002), “The mechanics of earthquake and faulting,” Cambridge University Press,
824 UK.

825

826 Steinberg, D.J.; Cochran, S.G.; Guinan, M.W. (1980), "A constitutive model for metals
827 applicable at high-strain rate", *Journal of Applied Physics* 51 (3): 1498, doi:10.1063/1.327799.
828

829 Sibson, R. H. (1973), Interaction between temperature and pore-fluid pressure during earthquake
830 faulting—A mechanism for partial or total stress relief, *Nature*, 243, 66–68.

831

832 Sone, H. & Shimamoto, T. *Nature Geosci.* 2, 705–708 (2009).

833

834 Tullis, T. E., and D. L. Goldsby (2003), Flash melting of crustal rocks at almost seismic slip
835 rates, Eos Trans. AGU, 84(46), Fall Meet. Suppl. Abstract S51B-05.

836

837

838

839

840

841

842

843

844

845

846

847

848

849

850

851

852 **Appendix: Estimation of the local increase in contact temperature**

853 In this appendix we derive Eqn. (11) and explain the numerical integration approach in the case
854 of multiple STZs.

855 The fundamental solution of the heat diffusion equation in one dimensional is given by:

856
$$\Phi(x, t) = \frac{1}{\sqrt{4\pi\alpha t}} \exp\left(-\frac{x^2}{4\alpha t}\right), \quad (\text{A.1})$$

857 where α is the thermal diffusion coefficient. For an arbitrary heat source $g(x, t)$, the
858 temperature distribution is obtained by convolving the heat source with the fundamental solution:

859
$$T(x, t) = \Phi(x, t) * g(x, t) = \int_0^t \int_{-\infty}^{\infty} \frac{1}{\sqrt{4\pi\alpha(t-t')}} \exp\left(-\frac{(x-y)^2}{4\alpha(t-t')}\right) g(y, t') dy dt'. \quad (\text{A.2})$$

860 For a planar heat source localized at the grains contact surface $g(x, t) = g_o(t) \delta(x)$. It follows
861 from the properties of delta function that:

862
$$T(x, t) = \int_0^t \frac{1}{\sqrt{4\pi\alpha(t-t')}} \exp\left(-\frac{x^2}{4\alpha(t-t')}\right) g_o(t') dt'. \quad (\text{A.3})$$

863 The maximum rise in temperature occurs at the contact; that is at $x = 0$. Hence,

864
$$T(0, t) = \int_0^t \frac{g_o(t')}{\sqrt{4\pi\alpha(t-t')}} dt' \quad (\text{A.4})$$

865 If we take $g_o(t) = s(t)V(t)/\rho c$, where ρc is the volumetric heat capacity, Eqn. (A.4) will reduce
 866 to Eqn. (11) in the text.

867 Equation (A.4) represents a convolution in time. At a given time t , the rise in temperature is due
 868 to the combined effects of all heat sources acting in the time period $0 \leq t' < t$. Explicitly,

$$\begin{aligned}
 T(0,t) = & \frac{g_o(0)}{\sqrt{4\pi\alpha(t-0)}} \Delta t_1 + \frac{g_o(\Delta t_1)}{\sqrt{4\pi\alpha(t-\Delta t_1)}} \Delta t_2 + \frac{g_o(\Delta t_1 + \Delta t_2)}{\sqrt{4\pi\alpha(t-\Delta t_1 - \Delta t_2)}} \Delta t_3 + \dots \\
 & + \frac{g_o\left(\sum_{i=0}^{n-1} \Delta t_i\right)}{\sqrt{4\pi\alpha\left(t - \sum_{i=0}^{n-1} \Delta t_i\right)}} \Delta t_n.
 \end{aligned} \tag{A.5}$$

870 In Eqn. (A.5), Δt_i is the time duration for which the heat source $g_o(\Delta t_{i-1})$ is active, and we let

871 $g(\Delta t_0) = g_o(0)$. We use the fact that $\sum_{i=0}^n \Delta t_i = t$. In this paper Δt_i is less than or equal to the time
 872 step required for integrating the STZ equations.

873 In deriving Eqn. (A.4) the limits of integration were taken as 0 and t . A contact surface, however,
 874 does not sense the effect of heat sources that operated before the contact exists. Furthermore, it
 875 will not increase in temperature after the grains lose contact. Hence, the limits of integration in
 876 this case correspond to the beginning and end of the contact lifetime. In case the contact slip rate
 877 is not constant, Eqn. (14) must be used to determine the contact lifetime.

878 We calculate the increase in temperature for all STZs. We record the highest contact temperature
 879 only since it controls the flow stress in the system. Once the STZ with the highest temperature
 880 completes its slip, we consider the next STZ in the hierarchy, i.e. the STZ with the second

881 highest temperature. We track the temperature evolution for this STZ until it completes its slip.

882 We repeat this for all remaining STZs.

883

884

885

886

887

888

889

890

891

892

893

894

895

896

897

898

Figures

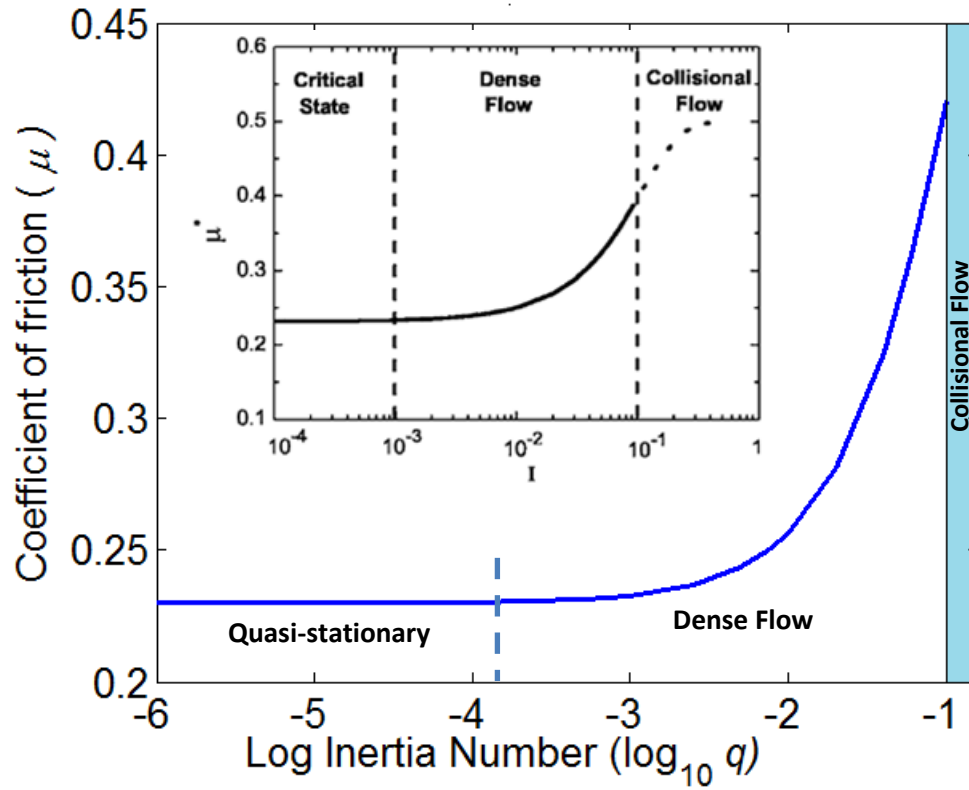


Fig. 1: Predictions of STZ theory for the rheology of sheared granular system with no local viscoplasticity at grain contacts. Insert shows results from molecular dynamic simulations [da Cruz et al., 2005, reprinted with permission]. [Simulations are shown for $s_o/s_c = 0.23$, $\varepsilon = 1$, $\chi_o = 0.2$].

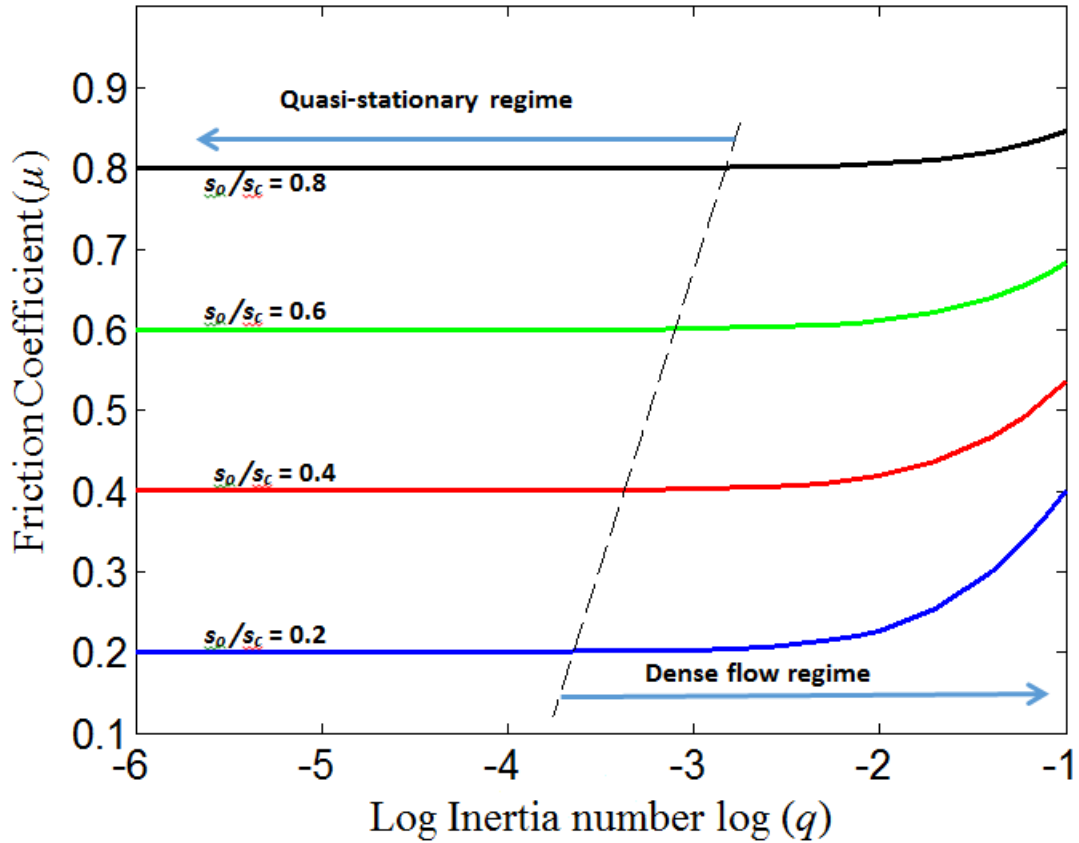


Fig. 2: Variation of coefficient of friction μ as a function of inertia number q for different values of s_o normalized by the pressure s_c . Systems with higher s_o exhibit a transition from quasi-static to dense flow at higher strain rates. This transition is traced approximately by the dashed curve. The dense flow regime also has different strengthening rates for different values of s_o . [The same parameters are used here as in Fig. 1, but with different s_o/s_c ratios.]

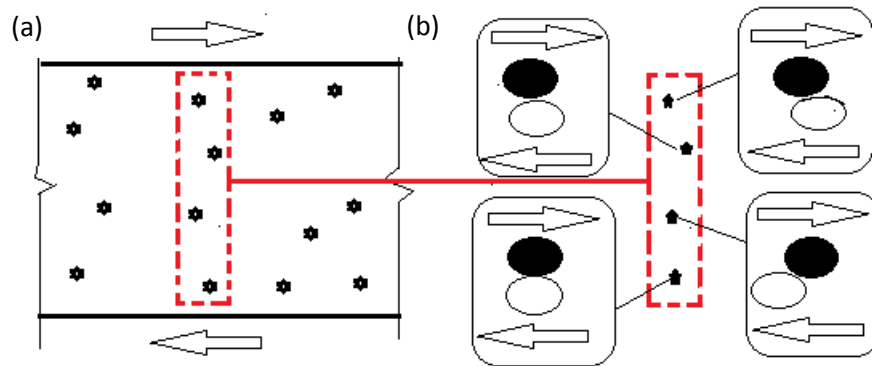


Fig. 3: A schematic for a 2D sheared granular layer with local plastic zones represented by stars. (a) The 2D representation. STZs are distributed along the depth as well as the width of the sample. The arrow represents the direction of shear. (b) The idealized 1D model assuming an infinite strip. Local plastic deformation is accommodated by inter particle slip as shown in the oval inserts. At any given instant, different particles are at different stages of their slip history.

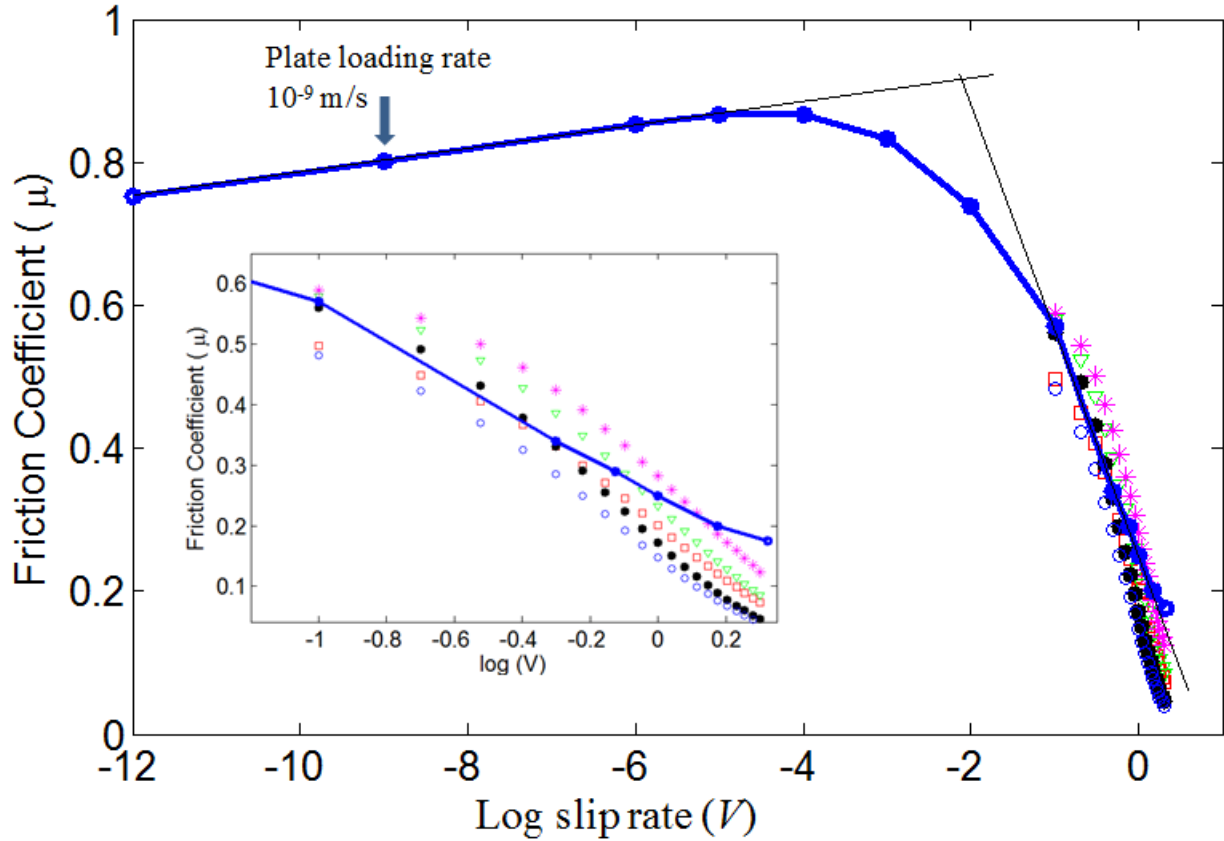


Fig. 4: Steady state friction coefficient as a function of slip rate (layer thickness = 1mm) at $T_b = 300$ K. Blue curve represents the prediction of our model based on Eqn. (9) for the grain contact strength. Scattered points represent the sweep of experimental data from Sone and Shimamoto [2009]. Different colors correspond to different values for the fitting parameters in Sone and Shimamoto [2009].

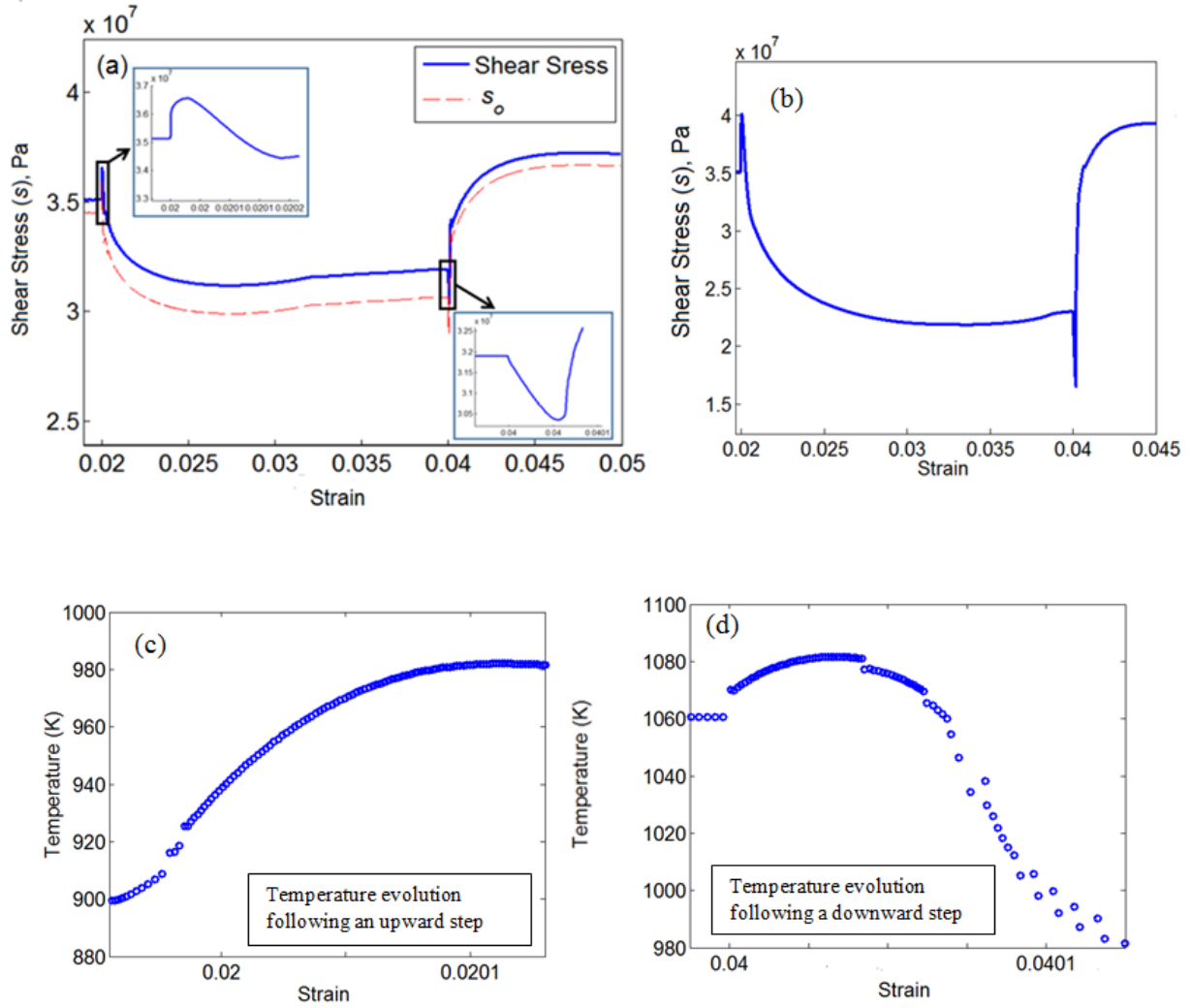


Fig. 5: Results for a velocity stepping numerical experiment. (a) Evolution of shear stress and minimum flow stress s_o . In the upward step, the strain rate is doubled. After steady state is reached the strain rate was reduced to its original value. Inserts show a magnified plot for the variation of shear stress immediately following the step. Steady state stress is reached after the downward step at strains greater than 0.05 (not shown here). (b) Evolution of shear stress in a pair of strain rate stepping experiment in which the strain rate ratio is 10 (0.1) in the upward (downward) step (respectively). (c) Evolution of contact temperature immediately following an upward step in velocity corresponding to Fig.(5a). (d) Evolution of contact temperature immediately following a downward step in velocity corresponding to Fig. (5a).

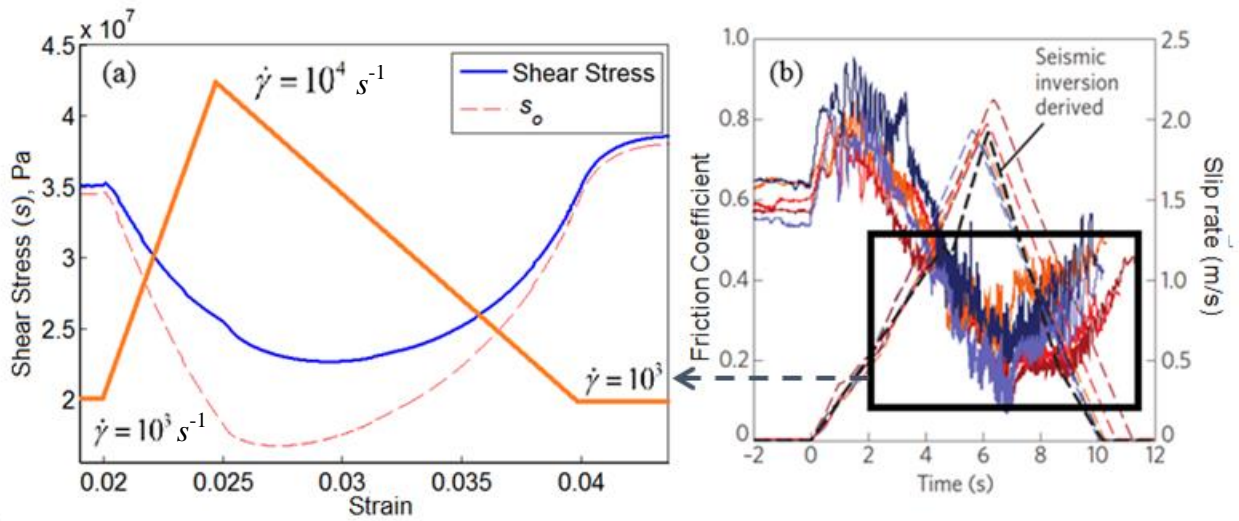


Fig. 6: Response to linear changes in imposed strain rates. (a) The model predicts gradual weakening followed by gradual strengthening as the velocity is ramped up then down. The brown solid line represents the velocity ramp (b) Experimental observations from Sone and Shimamoto [2009] (reprinted with permission) showing qualitatively similar behavior for the region within the black rectangle.

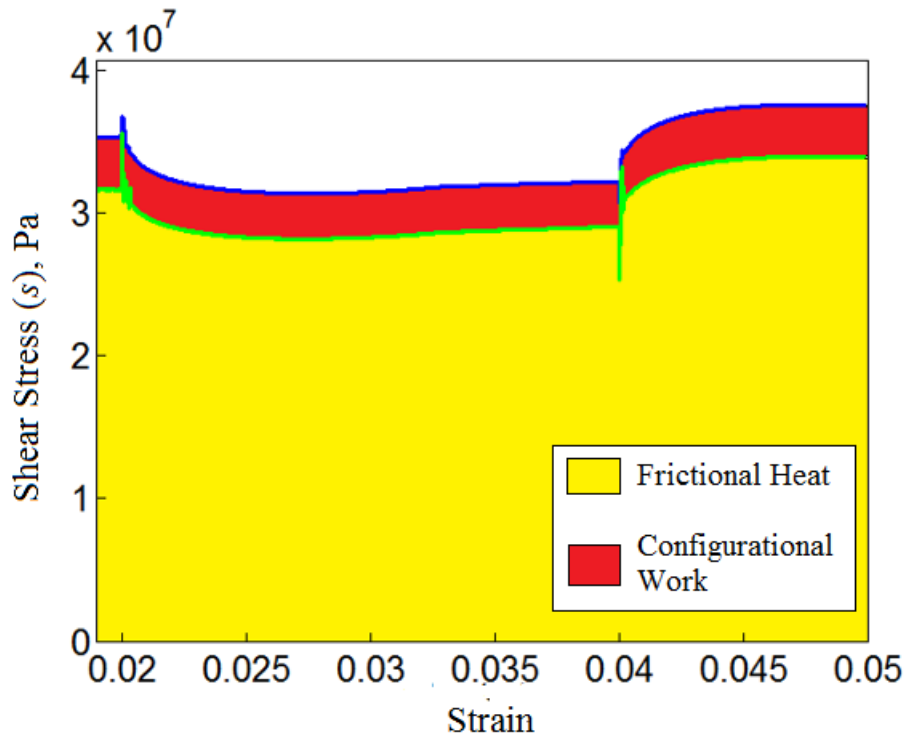


Fig. 7: Energy partitioning between frictional (yellow) and configurational (red) components. The blue line represents the macroscopic shear stress. The green line represents the fraction of the shear stress that is contributing to heat dissipation. For small strain, as shown here, the configurational energy is approximately 10% of the total energy budget. As slip further accumulates, the effective temperature evolves towards its steady state value and the fraction of energy consumed in increasing local disorder decreases. At steady state, all the external work is dissipated as heat.